Barycenter Calibration for MUSIC Spectrum of OFDM-ISAC Signals – A Super-Resolution Waveform Perspective

Meiyu Yin[1], Jingwen Li[1], Jialong Gong[1], Xiqing Liu[1(✉)], Mugen Peng[1], and Nian Xia[2]

[1] State Key Laboratory of Networking and Switching Technology, School of Information and Communication Engineering, Beijing University of Posts and Telecommunications, Beijing 100876, China
{yinmeiyu,lijingwen,yuri,liuxiqing,pmg}@bupt.edu.cn
[2] School of Computer and Electronic Information/School of Artificial Intelligence, Nanjing Normal University, Nanjing 210023, China
nian.xia@nnu.edu.cn

Abstract. The sixth-generation mobile communication system is expected to provide sensing services, and thus the integrated sensing and communication waveform has emerged as a hot research topic. In typical sensing systems, such as radar, sensing resolution is often constrained by available wireless resources. Achieving super-resolution sensing within the resource constraint poses a significant challenge. To this end, this work proposed a calibration algorithm for orthogonal frequency division multiplexing waveforms to conduct barycenter calibration (BC) of the multiple signal classification (MUSIC) spectrum that performs two-dimensional sensing. Simulation results demonstrated that the BC algorithm could significantly reduce sensing errors. Even at the edge of the MUSIC spectrum, it still exhibits robust performance. In addition, to comprehensively evaluate the performance gains, we introduce the capacity-to-error ratio and provide simulation results and discussions.

Keywords: Integrated sensing and communication · Barycenter calibration (BC) · Multiple signal classification · Orthogonal frequency division multiplexing

1 Introduction

The evolution of the sixth generation mobile communication system, known as 6G, envisions a network that integrates mobile communication and sensing func-

This work was supported in part by the National Key Research and Development Program of China (Grant No. 2021YFB2900200), in part by National Natural Science Foundation of China (Grant No. 62271085) and in part by Beijing Natural Science Foundation (Grant No. L223007-2).

H.-H. Chen and W. Meng (Eds.): WiSATS 2024, LNICST 606, pp. 89–105, 2025.
https://doi.org/10.1007/978-3-031-86203-8_8

tionalities. Sensing, in the broadest sense, encompasses the ability to perceive all aspects related to business, networking, users, terminals, and environmental object properties. A narrow definition of sensing stands for target localization, imaging, detection, identification, and tracking capabilities. High-precision sensing is a fundamental technology that serves futuristic applications. For example, use cases such as vehicle navigation, industrial infrastructure, emergency responders, and smart home, impose critical demands on range and velocity estimation.

Orthogonal frequency division multiplexing (OFDM) can effectively mitigate multipath effects and frequency-selective fading. However, designing integrated sensing and communication (ISAC) waveforms based on OFDM spectra for range and velocity estimation is challenging. Numerous research efforts have been devoted to developing waveforms for ISAC to address this challenge.

Sturm. C et al. in [1] first proposed the two-dimensional discrete Fourier transformation (2D-DFT) algorithm for jointly estimating range and velocity. A widely adopted method for improving resolution is to increase bandwidth. However, inherent bandwidth limitations impose constraints on resolution, which in turn adversely affect the accuracy of estimation performance. In response to this limitation, several pioneering research efforts have recently been undertaken to enhance sensing resolution. For example, R. Zhang et al. proposed a novel tensor-based approach in [2] to address channel estimation and target sensing problems with a unified framework in which parameters were estimated by the tensor-based algorithm uniformly. An OFDM signal represented in the frequency domain can be interpreted as a two-dimensional (2D) virtual array in a single snapshot, where the rows correspond to subcarriers and the columns represent symbols. Hence, in [3], a joint range-velocity estimator was implemented by the 2D multiple signal classification (MUSIC) algorithm for OFDM-based radar systems. Other algorithms, like Capon [4] and ESPRIT [5], can be employed to achieve high accuracy estimation with the improved resolution. OFDM can jointly estimate range and velocity since subcarriers and symbols in OFDM are associated with the target's range and Doppler, respectively. Compared to conventional smoothing, smoothing window optimization [6] could greatly enhance estimation accuracy while reducing computational cost. Due to bandwidth and power restrictions, spectrum calibration algorithms may be adopted to improve the accuracy of estimations. A two-stage search method was designed to refine the estimation process of the DFT spectrum peak. The process begins with a coarse search, followed by a more precise examination around the peak [7]. However, the resolution is limited to the spacing of the second stage. In [8], two samples on the DFT spectrum were utilized to finely estimate the peak based on a linear combination of unknown parameters, while [9] used three samples based on nonlinear relations. [10–12] used three samples to find the peak value. Although the above mentioned calibration algorithms are designed for frequency, amplitude, and phase estimation, they can also be adopted for spectrum peak search of MUSIC. The barycenter calibration (BC) algorithm can flexibly adjust the number of samples to estimate the peak value. In [13], the barycenter calibration algorithm was first suggested for OTFS delay-Doppler spectrum estima-

tion. Windowed high-order OTFS delay-Doppler spectrum can also be assisted by BC [14]. BC was proved to be effective for direction-of-arrival estimation with Capon/MUSIC algorithms in [15]. As far as we are aware, the BC algorithm has not been utilized in the context of OFDM. Furthermore, current BC solutions do not deal with the case where the peak value falls near the edge.

This work addresses the constraints on sensing resolution imposed by available wireless resources and demonstrates that the proposed BC-MUSIC OFDM scheme can significantly reduce range and velocity estimation errors, achieving super-resolution sensing. Particularly, this work first investigates how to calibrate the spectral barycenter near the observation edge, and we name this algorithm barycenter calibration with edge spectra (BCE). Owing to the algorithm's minimal complexity, it is expected to support real-time requirements in 6G ISAC services.

This paper is structured as follows: Sect. 2 introduces the system model for an OFDM-ISAC transceiver. The principle underlying the simultaneous estimation of range and velocity, along with an explanation of the BCE algorithm, is covered in Sect. 3. Section 4 focuses on analyzing the performance of the CRLB. In Sect. 5, we present the outcomes of the simulations, discussing their implications. Finally, Sect. 6 wraps up the discussion with concluding remarks.

2 System Model

Figure 1 depicts a configuration where the transmitter and receiver are jointly allocated for communication and sensing purposes. After the ISAC signal is transmitted, communication users receive it through downlink communication channels, and communication users transmit data to the communication receiver through uplink channels. The ISAC signal transmitted will bounce off multiple targets, with the echo signal subsequently returning to the sensing receiver. The symbol $\mathcal{K}$ represents the total count of targets. For every target, the distance to the receiver is denoted as d_k, while the relative velocity concerning the kth target is represented by v_k.

2.1 Integrated Transmitter

The diagram depicting the structure of the OFDM-ISAC transceiver can be found in the transmitter section of Fig. 1. Within the transmitter, a bit sequence of length $(\log_2 \mathcal{M} \times MN)$ is produced by the information source, represented as $\mathbf{o}_{1\times[(\log_2 \mathcal{M})\times MN]}$, $\mathbf{o}(i) \in \{0,1\}, i = 1,2,\cdots,(\log_2 \mathcal{M}) \times MN$. The term MN indicates the total number of symbols within an OFDM frame. Following this, the bits contained in $\mathbf{o}$ are mapped to $\mathcal{M}$-ary quadrature amplitude modulation (QAM) symbols through the use of a modulation alphabet $\mathbb{B} = \{\mathcal{B}_1, \mathcal{B}_2, \cdots, \mathcal{B}_{\mathcal{M}}\}$, which results in the formation of the modulated symbol vector $\mathbf{a}_{1\times(MN)}$. After modulation, we can achieve a symbol train, denoted as $\mathbf{a} \triangleq [\mathbf{a}_1^T, \cdots, \mathbf{a}_m^T, \cdots, \mathbf{a}_M^T]_{1\times(MN)}$, in which $\mathbf{a}_m^T$ is defined as

$\mathbf{a}_m^T \triangleq [a_{m,1}, \cdots, a_{m,n}, \cdots, a_{m,N}]$. Next, the symbol train is fed into a serial-to-parallel converter (S/P), yielding a symbol matrix, which can be written into

$$\mathbf{A} \triangleq \begin{bmatrix} \mathbf{a}_1^T \\ \vdots \\ \mathbf{a}_m^T \\ \vdots \\ \mathbf{a}_M^T \end{bmatrix} = \begin{bmatrix} a_{1,1} & \cdots & a_{1,n} & \cdots & a_{1,N} \\ \vdots & \ddots & & & \vdots \\ a_{m,1} & & a_{m,n} & & a_{m,N} \\ \vdots & & & \ddots & \vdots \\ a_{M,1} & \cdots & a_{M,n} & \cdots & a_{M,N} \end{bmatrix}_{M \times N} \tag{1}$$

Subsequently, the transformation of the symbol matrix from the frequency domain to the time domain occurs via the inverse fast Fourier transform (IFFT), represented by $\mathbf{X} = \mathbf{F}^{-1}\mathbf{A}$, where $\mathbf{X}_{M \times N}$ refers to the transmitted symbol matrix in the time domain.

Next, the $\mathbf{X}$ is fed into a parallel-to-serial converter (P/S), reshaped into a symbol vector $\mathbf{x} \triangleq [\mathbf{x}_1^T, \cdots, \mathbf{x}_m^T, \cdots, \mathbf{x}_M^T]_{1 \times (MN)}$, where $\mathbf{x}_m^T$ denotes the symbol vector transmitted on the mth subcarrier. Afterwards, to avoid inter-symbol interference, the cyclic prefix is added to the symbol vector, described as $\tilde{\mathbf{x}} \triangleq [\tilde{\mathbf{x}}_1^T, \cdots, \tilde{\mathbf{x}}_m^T, \cdots, \tilde{\mathbf{x}}_M^T]_{1 \times [(M+\mu)N]}$, where μ is the cyclic prefix length. Each digital symbol in the symbol vector should be transformed into an analog signal by digital-to-analog (D/A) for subsequent RF modulation, namely multiplying a rectangular window. The analog signal is $\tilde{x}(t) = \tilde{\mathbf{x}}[i] * \mathrm{rect}(\frac{t - iT_B}{T_B})$, where $i (i = 1, \ldots, (M+\mu)N)$ is the index of the element of $\tilde{\mathbf{x}}$, $T_B = 1/(M\Delta f)$ equals to the time interval of sampling; Δf is the subcarrier spacing. Also, the duration of a complete OFDM symbol is $T_s = T + T_{\mathrm{cp}}$, where $T = 1/\Delta f$ is the duration of an OFDM symbol; T_{cp} is the duration of the cyclic prefix. Then, the signal is modulated to RF signal $x(t)$ with carrier frequency f_c.

2.2 Channel

The channel impulse response is formulated as

$$h(t, \tau) = \sum_{k=1}^{\mathcal{K}} \rho_k \delta(\tau - \tau_k) e^{j2\pi\nu_k t}, \tag{2}$$

where $\mathcal{K}$ represents the number of the multipath channels; ρ_k denotes the complex channel gain associated with the kth path; $\delta(\cdot)$ denotes the Dirac function. The delay τ_k and Doppler shift ν_k of the kth path are respectively given by

$$\tau_k = \frac{2d_k}{c}, \quad \nu_k = f_c \frac{2v_k}{c}, \tag{3}$$

where d_k and v_k represent the relative distance and relative velocity of the kth path, respectively. The duration of the cyclic prefix $T_{\mathrm{cp}} \geq \tau_k$, $k = 1, \ldots, \mathcal{K}$.

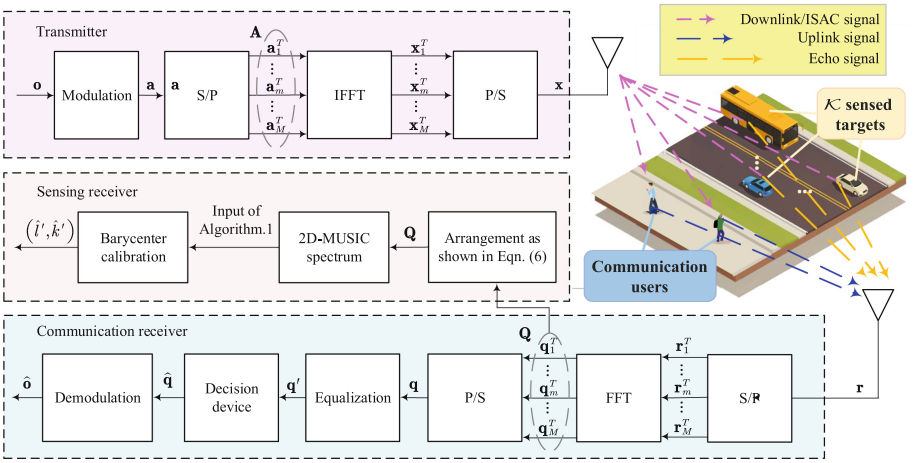

Fig. 1. System model of the downlink OFDM-ISAC system. The ISAC signal is generated by the base station (BS). Then, it is captured by the communication users and reflected off $\mathcal{K}$ sensed targets. Besides, the BS is equipped with a communication receiver and a sensing receiver, which respectively decode the communication data from users and receive echo signals from targets.

2.3 Receiver

At the receiver module, we can observe from Fig. 1 the received signal, which may either be the user's communication signal or the echo reflected from a target, is handled concurrently by both the sensing and communication modules. The $\mathcal{K}$ point targets possess respectively the distance d_k and the relative velocity v_k, for $k = 1, \cdots, \mathcal{K}$. The velocity of the kth target satisfies $2v_k \ll c$, and c is the speed of light.

The received signal should first be down-converted to a baseband signal, given by

$$r(t) = e^{-j2\pi f_c t} \int h(t,\tau)x(t-\tau)\mathrm{d}\tau. \tag{4}$$

Then, sampling the received signal $r(t)$ and removing the CP, we can achieve the sequence, $\mathbf{r} \triangleq [\mathbf{r}_1^T, \cdots, \mathbf{r}_n^T, \cdots, \mathbf{r}_N^T]$, $n = 1, 2, \cdots, N$, in which $\mathbf{r}_n^T$ can be expressed as

$$\mathbf{r}_n^T \triangleq [r_{\mu+1,n}, \cdots, r_{m+\mu,n}, \cdots, r_{M+\mu,n}], \tag{5}$$

where $m\,(m = 1, \cdots, M)$ denotes the sample index; μ is the length of CP; $r_{i,j}$ is the $[(j-1)(M+\mu)+i]$th sample of $r(t)$, given by $r_{i,j} = r((j-1)T_s + i/(M\Delta f))$.

Communication Receiver. As shown in Fig. 1, the received data vector is transformed into a matrix by S/P, as described $\mathbf{R} \triangleq [\mathbf{r}_1, \cdots, \mathbf{r}_m, \cdots, \mathbf{r}_M]$. After that, the symbol matrix $\mathbf{R}$ in the time domain is converted into $\mathbf{Q}$ in the frequency domain using the Fast Fourier Transform (FFT), represented by the

equation $\mathbf{Q} = \mathbf{FR}$, where $\mathbf{Q}$ is defined as $\mathbf{Q} \triangleq [\mathbf{q}_1, \cdots, \mathbf{q}_m, \cdots, \mathbf{q}_M]$. By P/S, the matrix $\mathbf{Q}$ is reshaped into a vector $\mathbf{q} \triangleq [\mathbf{q}_1^T, \cdots, \mathbf{q}_m^T, \cdots, \mathbf{q}_M^T]$. Equalizer follows up to remove the gains yielded by the channel, $\mathbf{q}' = \mathbf{H}^{-1}\mathbf{q}$, where $\mathbf{H}^{-1}$ denotes the inverse matrix of the channel matrix. Next, decision is conducted to obtain $\hat{\mathbf{q}} \triangleq f(\mathbf{q}')$, where function f denotes the decision device rule. Finally, the recovered symbol vector $\hat{\mathbf{q}}_{1\times(MN)}$ is demapped into a bit sequence $\hat{\mathbf{o}}_{1\times[(\log_2 \mathcal{M})\times MN]}$, $\hat{\mathbf{o}}(i) \in \{0, 1\}$, $i = 1, 2, \cdots, (\log_2 \mathcal{M}) \times MN$.

Sensing Receiver. As the echo signal is transmitted and received in co-allocation, the transmit matrix $\mathbf{A}$ is known to the sensing receiver [6]. As shown in Fig. 1, the received echo matrix is

$$\mathbf{Q} = \begin{bmatrix} q_{1+\mu,1} & \cdots & q_{1+\mu,n} & \cdots & q_{1+\mu,N} \\ \vdots & \ddots & & & \vdots \\ q_{m+\mu,1} & & q_{m+\mu,n} & & q_{m+\mu,N} \\ \vdots & & & \ddots & \vdots \\ q_{M+\mu,1} & \cdots & q_{M+\mu,n} & \cdots & q_{M+\mu,N} \end{bmatrix}_{M\times N} = \tilde{\mathbf{X}} + \mathbf{N} = \mathbf{H}(\mathbf{d}, \mathbf{v}) \odot \mathbf{A} + \mathbf{N}, \tag{6}$$

where the element is derived by

$$q_{m+\mu,n} = a_{m,n} \sum_{k=1}^{\mathcal{K}} \rho_k e^{-j2\pi m \Delta f \frac{2d_k}{c}} e^{j2\pi n T_s \frac{f_c 2v_k}{c}} + n_{m,n} = \hat{x}_{m,n} + n_{m,n}, \tag{7}$$

where $m (m = 1, 2, \cdots, M)$ and $n (n = 1, 2, \cdots, N)$ are the indices of sub-carriers and symbol block, respectively. Also, $\mathbf{d}$ and $\mathbf{v}$ are defined as $\mathbf{d} \triangleq [d_1, \cdots, d_k, \cdots, d_{\mathcal{K}}]$, $\mathbf{v} \triangleq [v_1, \cdots, v_k, \cdots, v_{\mathcal{K}}]$, where d_k and v_k denote the range and velocity of the kth target, respectively. The noise $\mathbf{N}$ is a $M \times N$ matrix; "$\odot$" denotes the Hadamard product. Let $\mathbf{\Upsilon} = [\rho_1, \cdots, \rho_k, \cdots, \rho_{\mathcal{K}}]^T$, and the channel matrix can be decomposed as

$$\mathbf{H}(\mathbf{d}, \mathbf{v}) = \sum_{k=1}^{\mathcal{K}} e^{j2\pi n T_s \frac{f_c 2v_k}{c}} \rho_k e^{-j2\pi m \Delta f \frac{2d_k}{c}} = \mathbf{U}(\mathbf{d}) \mathrm{diag}(\mathbf{\Upsilon}) \mathbf{B}(\mathbf{v})^T. \tag{8}$$

The matrices of the phase shift due to the delay and Doppler are respectively defined as

$$\begin{cases} \mathbf{U}(\mathbf{d}) \triangleq [\mathbf{u}(d_1), \cdots, \mathbf{u}(d_k), \cdots, \mathbf{u}(d_{\mathcal{K}})], \\ \mathbf{B}(\mathbf{v}) \triangleq [\mathbf{b}(v_1), \cdots, \mathbf{b}(v_k), \cdots, \mathbf{b}(v_{\mathcal{K}})], \end{cases} \tag{9}$$

where $\mathbf{u}(d_k) = [1, u(d_k), \cdots, u^{M-1}(d_k)]^T$, and $u(d_k) = e^{-j2\pi\Delta f \frac{2d_k}{c}}$; $\mathbf{b}(v_k) = [1, b(v_k), \cdots, b^{N-1}(v_k)]^T$, and $b(v_k) = e^{j2\pi f_c \frac{2v_k}{c} T_s}$.

It is necessary to eliminate the influence of the transmit matrix $\mathbf{A}$ from $\mathbf{Q}$ using element-wise division. The resulting covariance matrix of this division is regarded as the matrix yielded in the 2D-MUSIC algorithm to perform the two-dimensional spectrum, as discussed in detail in Sect. 3.1. The range and velocity

estimates achieved by 2D-MUSIC can be further refined through the barycenter calibration algorithm, which will be discussed in detail in Sect. 3.2. The outcomes of this process are discrete indices that will subsequently be converted into range and velocity.

3 Joint Range and Velocity Estimation

To begin this section, we will outline the procedure for generating the 2D-MUSIC spectrum. Subsequently, we introduce the BCE algorithm, which involves a detailed explanation of the processing method for points located near the spectrum edge or elsewhere.

3.1 MUSIC Spectrum

Range and velocity are jointly estimated through the 2D-MUSIC algorithm. The matrix $\mathbf{O}$ is derived by element-wise division of the transmit matrix from the received matrix:

$$(\mathbf{O})_{(m,n)} = (\mathbf{Q})_{(m,n)}/(\mathbf{A})_{(m,n)} = (\mathbf{H})_{(m,n)} + (\tilde{\mathbf{N}})_{(m,n)}, \tag{10}$$

where $(\tilde{\mathbf{N}})_{(m,n)} \triangleq (\mathbf{N})_{(m,n)}/(\mathbf{A})_{(m,n)}$ denotes the noise matrix. The steering vector is derived by $\mathbf{c}(d,v) = \mathbf{b}(v) \otimes \mathbf{u}(d) \in \mathbb{C}^{(NM)\times 1}$, where "$\otimes$" denotes the Kronecker product. Reshape the matrix $\mathbf{O}$ into

$$\mathbf{Y}_{(MN)\times 1} = \mathrm{vec}(\mathbf{O}_{M\times N}) = \sum_{k=1}^{\mathcal{K}} \rho_k \mathbf{c}(d_k, v_k) + \mathrm{vec}(\tilde{\mathbf{N}}_{M\times N}), \tag{11}$$

where $\mathrm{vec}(\cdot)$ refers to column vectorization. Typically, the MUSIC algorithm is used for direction-of-angle estimation. Thus, the matrix $\mathbf{Y}$ can be equivalent to an array matrix with the number of antennas to be $N_L = NM$ and the number of snapshots to be $N_{\mathrm{snap}} = 1$. Covariance matrix $\mathbf{O}_{\mathbf{xx}}$ of reshaped matrix $\mathbf{Y}$ can be decomposed into

$$\mathbf{O}_{\mathbf{xx}} = \frac{1}{N_{\mathrm{snap}}} \mathbf{Y}\mathbf{Y}^H = \hat{\mathbf{E}}\mathbf{\Lambda}\hat{\mathbf{E}}^H, \tag{12}$$

where $\mathbf{\Lambda} = \mathrm{diag}(\lambda_1, \lambda_2, \cdots, \lambda_{N_L})$ represents the diagonal matrix of eigenvalues for $\mathbf{O}_{\mathbf{xx}}$; λ_j and $\mathbf{S}_j$ are eigenvalue and corresponding eigenvector of $\mathbf{O}_{\mathbf{xx}}$, respectively for $j = 1, 2, \cdots, N_L$, and $\hat{\mathbf{E}} = [\mathbf{S}_1, \mathbf{S}_2, \cdots, \mathbf{S}_{N_L}]$. Calculate eigenvalues of $\mathbf{O}_{\mathbf{xx}}$ and sort them in the order of $\lambda_1 \geq \lambda_2 \cdots \geq \lambda_{\mathcal{K}} \gg \lambda_{\mathcal{K}+1} \geq \cdots \geq \lambda_{N_L}$, where the first $\mathcal{K}$ maximum eigenvalues refer to signal eigenvalues, and the last $N_L - \mathcal{K}$ minimum eigenvalues refer to noise eigenvalues. Mathematically, we can express them as

$$\begin{cases} \hat{\mathbf{E}}_s = [\hat{\mathbf{S}}_1, \hat{\mathbf{S}}_2, \cdots, \hat{\mathbf{S}}_{\mathcal{K}}], \\ \hat{\mathbf{E}}_n = [\hat{\mathbf{S}}_{\mathcal{K}+1}, \hat{\mathbf{S}}_{\mathcal{K}+2}, \cdots, \hat{\mathbf{S}}_{N_L}]. \end{cases} \tag{13}$$

Based on operations and the decomposition above, the spectrum of MUSIC is calculated by

$$\tilde{\mathrm{P}}_{\mathrm{music}}(d,v) \triangleq \frac{1}{\mathbf{c}^H(d,v)\hat{\mathbf{E}}_n\hat{\mathbf{E}}_n^H\mathbf{c}(d,v)}. \tag{14}$$

Then the sampled MUSIC spectrum, $\mathrm{P}_{\mathrm{music}}(n_d,n_v)$, can be obtained by

$$\mathrm{P}_{\mathrm{music}}(n_d,n_v) \triangleq \tilde{\mathrm{P}}_{\mathrm{music}}\left(\frac{cn_d}{2\Delta f d_h},\frac{cn_v}{2f_cT_sv_h}\right), \tag{15}$$

where $n_d(n_d=d_l,\cdots,d_h)$ and $n_v(n_v=v_l,\cdots,v_h)$ are the indices of range and velocity dimension on the sampled MUSIC spectrum, respectively; d_h-v_l and v_h-v_l are the number of samples N_s on MUSIC spectrum $\tilde{\mathrm{P}}_{\mathrm{music}}(d,v)$ along the range and velocity dimension, respectively. The observed peak of the sampled MUSIC spectrum corresponds to the integer index of range and velocity:

$$[\mathring{d},\mathring{v}] \triangleq \arg\max_{n_d,n_v}\mathrm{P}_{\mathrm{music}}\left(n_d,n_v\right). \tag{16}$$

3.2 Barycenter Calibration Algorithm

Due to the picket fence effect, the observed range and velocity, denoted as $\mathring{d}$ and $\mathring{v}$, respectively, are identified as the nearest integer indices to the actual peak. The BC algorithm is employed to estimate an fraction index closer to the actual peak within an area around the observed peak $\mathring{d},\mathring{v}$, whose dimension is $N_d\times N_v$. Here, N_d and N_v represent the count of observation points along the range and velocity axes, respectively. It is important to mention that, in this study, the observation area is considered square ($N_d=N_v$), and N_d and N_v are both even numbers unless otherwise specified.

The observation area should be as symmetrical around the actual peak as possible. Next, we will explain how to select observation points. In the range dimension, two approximate points $\mathrm{P}_{\mathrm{music}}(\mathring{d}-1,\mathring{v})$ and $\mathrm{P}_{\mathrm{music}}(\mathring{d}+1,\mathring{v})$ are chosen on each side of $\mathring{d}$. If $\mathrm{P}_{\mathrm{music}}(\mathring{d}-1,\mathring{v})$ is greater than $\mathrm{P}_{\mathrm{music}}(\mathring{d}+1,\mathring{v})$, the actual peak falls between $\mathring{d}-1$ and $\mathring{d}$, and then the range observation points are in order of $\mathring{d},\mathring{d}-1,\mathring{d}+1,\mathring{d}-2,\cdots,\mathring{d}-N_d/2$; if $\mathrm{P}_{\mathrm{music}}(\mathring{d}-1,\mathring{v})$ is smaller than $\mathrm{P}_{\mathrm{music}}(\mathring{d}+1,\mathring{v})$, the actual peak falls between $\mathring{d}+1$ and $\mathring{d}$, and then the range observation points are in order of $\mathring{d},\mathring{d}+1,\mathring{d}-1,\mathring{d}+2,\cdots,\mathring{d}+N_d/2$. Observation points are selected in the velocity dimension similarly.

To simplify mathematical expression, function $\varphi_d(i)$ and $\varphi_v(j)$ are defined as [13]

$$\varphi_d(i)=\begin{cases}\dfrac{(-1)^{i+1}[i-\frac{1-(-1)^i}{2}]}{2}, & \text{for } \mathrm{P}_{\mathrm{music}}(\mathring{d}-1,\mathring{v})\geqslant\mathrm{P}_{\mathrm{music}}(\mathring{d}+1,\mathring{v}),\\ \dfrac{(-1)^{i}[i-\frac{1-(-1)^i}{2}]}{2}, & \text{for } \mathrm{P}_{\mathrm{music}}(\mathring{d}-1,\mathring{v})<\mathrm{P}_{\mathrm{music}}(\mathring{d}+1,\mathring{v}),\end{cases} \tag{17}$$

$$\varphi_v(j) = \begin{cases} \dfrac{(-1)^{j+1}[j - \frac{1-(-1)^j}{2}]}{2}, & \text{for } \mathrm{P}_{\text{music}}(\mathring{d}, \mathring{v}-1) \geqslant \mathrm{P}_{\text{music}}(\mathring{d}, \mathring{v}+1), \\ \dfrac{(-1)^{j}[j - \frac{1-(-1)^j}{2}]}{2}, & \text{for } \mathrm{P}_{\text{music}}(\mathring{d}, \mathring{v}-1) < \mathrm{P}_{\text{music}}(\mathring{d}, \mathring{v}+1), \end{cases} \tag{18}$$

where $i (i = 1, \cdots, N_d)$ and $j (j = 1, \cdots, N_v)$ are the indices of observation area along range and velocity axes, respectively. The observation area is expressed by a matrix $\hat{\mathbf{G}}[i,j] = \mathrm{P}_{\text{music}}(\mathring{d} + \varphi_d(i), \mathring{v} + \varphi_v(j))$. We can calculate the range index after calibration as

$$\hat{l}' = \frac{\sum_{i=1}^{N_d}\sum_{j=1}^{N_v}(\mathring{d} + \varphi_d(i))\hat{\mathbf{G}}[i,j]}{\sum_{i=1}^{N_d}\sum_{j=1}^{N_v}\hat{\mathbf{G}}[i,j]} \tag{19}$$

And the velocity index after calibration is computed as

$$\hat{k}' = \frac{\sum_{i=1}^{N_d}\sum_{j=1}^{N_v}(\mathring{v} + \varphi_v(j))\hat{\mathbf{G}}[i,j]}{\sum_{i=1}^{N_d}\sum_{j=1}^{N_v}\hat{\mathbf{G}}[i,j]} \tag{20}$$

Algorithm 1. Barycenter Calibration with Edge

Input: 2D-MUSIC spectrum $\mathrm{P}_{\text{music}}(n_d, n_v)$, size of the observation zone $N_d \times N_v$, number of the sensed targets $\mathcal{K}$;

Output: Estimated range $\hat{l}'$, and velocity $\hat{k}'$.

Find the $\mathcal{K}$ peaks of the 2D-MUSIC spectrum $\mathrm{P}_{\text{music}}(n_d, n_v)$
for $1 \leq k \leq \mathcal{K}$ **do**
  $[\mathring{d}, \mathring{v}] \leftarrow \arg\max_{n_d, n_v} \mathrm{P}_{\text{music}}(n_d, n_v)$
  Determine function $\varphi_d(i)$ according to 17 and function $\varphi_v(j)$ according to 18.
  if $0 \leq \mathring{d} + \varphi_d(i) \leq d_h$ and $0 \leq \mathring{v} + \varphi_v(i) \leq v_h$ **then**
    $\hat{\mathbf{G}}[i,j] \leftarrow \mathrm{P}_{\text{music}}(\mathring{d} + \varphi_d(i), \mathring{v} + \varphi_v(j))$
  else
    $\mathring{d} + \varphi_d(i) \leftarrow d_l + \mathrm{mod}(\mathring{d} + \varphi_d(i), d_h)$
    $\mathring{v} + \varphi_v(i) \leftarrow v_l + \mathrm{mod}(\mathring{v} + \varphi_v(i), v_h)$
  end if
  $\hat{l}' \leftarrow \frac{\sum_{i=1}^{N_d}\sum_{j=1}^{N_v}(\mathring{d}+\varphi_d(i))\hat{\mathbf{G}}[i,j]}{\sum_{i=1}^{N_d}\sum_{j=1}^{N_v}\hat{\mathbf{G}}[i,j]}$
  $\hat{k}' \leftarrow \frac{\sum_{i=1}^{N_d}\sum_{j=1}^{N_v}(\mathring{v}+\varphi_v(j))\hat{\mathbf{G}}[i,j]}{\sum_{i=1}^{N_d}\sum_{j=1}^{N_v}\hat{\mathbf{G}}[i,j]}$
  return $\hat{l}'$, $\hat{k}'$
end for

For the 2D-MUSIC spectrum, as shown in Fig. 2(a), lower and upper edge of ranges are placed along the range axis on each side of the scope, and lower and upper edge of velocity are placed along the velocity axis on each side of the scope. The range index varies in $\{d_l, d_l+1, d_l+2, \cdots, d_h\}$ and the velocity index varies

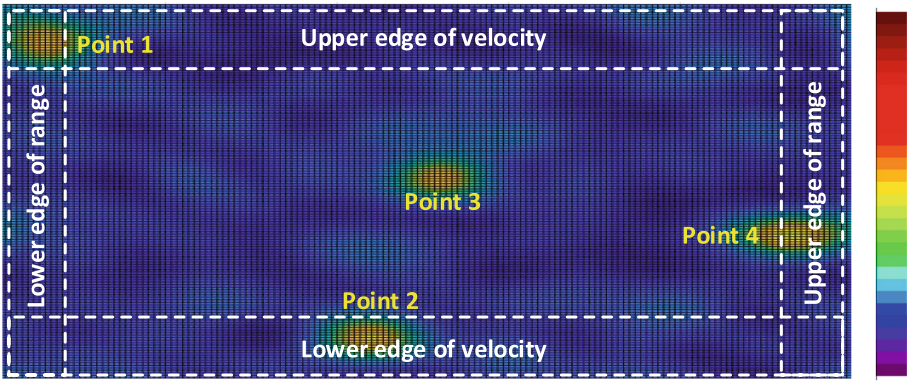

(a) Illustration of 2D-MUSIC spectrum and edge area, where four points fall into different areas.

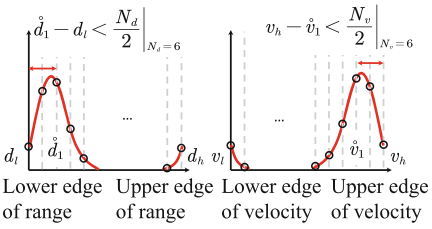

(b) MUSIC spectrum for Point 1.

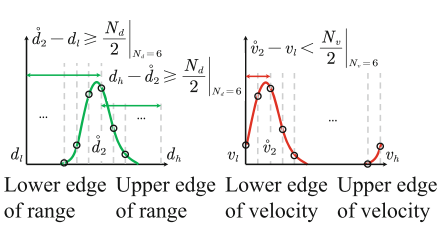

(c) MUSIC spectrum for Point 2.

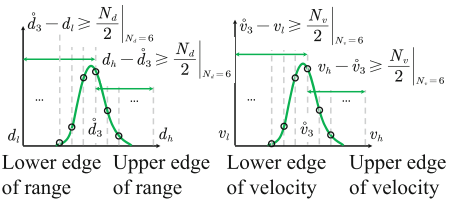

(d) MUSIC spectrum for Point 3.

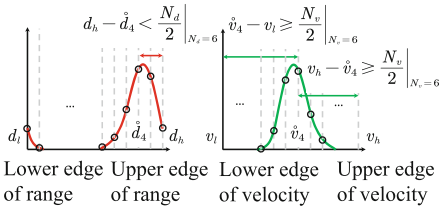

(e) MUSIC spectrum for Point 4.

Fig. 2. Illustration of edge areas. Four different spectrum cases for points falling into different edge areas. The size of observation area is set as $N_d \times N_v = 6 \times 6$. $\mathring{d}_k$ and $\mathring{v}_k$ are the integer closest indices to the kth actual peak value, for $k = 1, 2, 3, 4$. d_h, v_h are the highest indices along the range and velocity dimensions, respectively. d_l, v_l are the lowest indices along the range and velocity dimensions, respectively. $d_h - d_l$ equals the number of samples N_s.

in $\{v_l, v_l + 1, v_l + 2, \cdots, v_h\}$. Define *range or velocity falls near the edge* when $\mathring{d}+\varphi_d(i) < d_l$ or $\mathring{d}+\varphi_d(i) > d_h$ or $\mathring{v}+\varphi_v(j) < v_l$ or $\mathring{v}+\varphi_v(i) > v_h$. As depicted in Fig. 2(a), edge area is enclosed by four white dashed rectangles. When range or velocity falls near the edge, typical barycenter calibration algorithm can not take effect. Performance near edge area degrades back to integer closest estimation.

To deal with such situation, this work proposed an algorithm to enhance the estimation accuracy of points falling near edges. In (7), phase shift due to delay and Doppler are expressed respectively as $-2\pi m\Delta f\frac{2d}{c}$ and $2\pi nT_s\frac{f_c 2v}{c}$, which both vary in $[0, 2\pi]$. Due to periodicity of phase shift, when range or velocity falls near the edge, the observation points required falling outside of the edge can be replaced by points of the opposite side, as the red spectra depicted in Fig. 2. The substitution is achieved by $d_l + \mathrm{mod}(\mathring{d} + \varphi_d(i), d_h - d_l)$ and $v_l + \mathrm{mod}(\mathring{v} + \varphi_v(j), v_h - v_l)$, where "mod" denotes modulo operator. The whole process of BCE algorithm in pseudocode is demonstrated in Alg. 1.

In Fig. 2(a), four points represent four different cases and points fall into different edge areas. Assume that $\mathring{d}_k$ and $\mathring{v}_k$ represent the range and velocity indices of kth point, respectively, for $k = \{1, 2, 3, 4\}$. Figure 2(b) illustrates Point 1, which is not only near either edge of range but also either edge of velocity, on condition that $\mathring{d}_1 - d_l < \frac{N_d}{2}$ and $\mathring{v}_1 - v_l < \frac{N_v}{2}$. Figure 2(c) illustrates Point 2, which is only near either edge of velocity, on condition that $\mathring{d}_2 - d_l \geq \frac{N_d}{2}$, $d_h - \mathring{d}_2 \geq \frac{N_d}{2}$, and $\mathring{v}_2 - v_l < \frac{N_v}{2}$. Figure 2(d) illustrates Point 3, which is near neither edge of range or velocity if $\mathring{d}_3 - d_l \geq \frac{N_d}{2}$, $d_h - \mathring{d}_3 \geq \frac{N_d}{2}$, $\mathring{v}_3 - v_l \geq \frac{N_v}{2}$, and $v_h - \mathring{v}_3 \geq \frac{N_v}{2}$. Figure 2(e) illustrates Point 4, which is near either edge of ranges if $d_h - \mathring{d}_4 < \frac{N_d}{2}$, $\mathring{v}_4 - v_l \geq \frac{N_v}{2}$, and $v_h - \mathring{v}_4 \geq \frac{N_v}{2}$.

4 Performance Analysis

In this section, we derive the Cramér-Rao Lower Bounds (CRLB) for estimating range and velocity to assess the target sensing capabilities of the BCE algorithm. Additionally, the capacity-to-error ratio (CER) is employed to analyze the ISAC performance of the BCE algorithm.

4.1 Cramér-Rao Lower Bound

We define the target parameter set as $\boldsymbol{\theta} = [\mathbf{d}, \mathbf{v}]$, where $\mathbf{d} = [d_1, \cdots, d_k, \cdots, d_{\mathcal{K}}]$, $\mathbf{v} = [v_1, \cdots, v_k, \cdots, v_{\mathcal{K}}]$, with d_k and v_k denote the range and velocity of the target k, respectively. According to (6), the received samples can be expressed as

$$\tilde{q}_{m,n} \triangleq q_{m+\mu,n} = \hat{x}_{m,n} + n_{m,n}, \tag{21}$$

where $q_{m+\mu,n}$, $\hat{x}_{m,n}$ and $n_{m,n}$ represent the elements from matrices $\mathbf{Q}$, $\hat{\mathbf{X}}$ and $\mathbf{N}$, respectively. The received sample $q_{m+\mu,n}$ can be modeled as a random variable that adheres to a Gaussian distribution, with its mean at $\hat{x}_{m,n}$ and a variance of σ^2. The joint likelihood function is given by

$$\mathrm{P}(\mathbf{Q} \mid \boldsymbol{\theta}) = \prod_{n=1}^{N}\prod_{m=1}^{M}\frac{1}{\pi\sigma^2}e^{-\frac{|\tilde{q}_{m,n}-\hat{x}_{m,n}(\boldsymbol{\theta})|^2}{\sigma^2}}, \tag{22}$$

The Fisher information matrix $\mathbf{I}(\boldsymbol{\theta}) \in \mathbb{R}^{2\mathcal{K}\times 2\mathcal{K}}$ is then computed using the expression $[\mathbf{I}(\boldsymbol{\theta})]_{p,q} = -\mathrm{E}[\frac{\partial^2 \ln \mathrm{P}(\mathbf{Q}|\boldsymbol{\theta})}{\partial\theta_p \partial\theta_q}]$

$$[\mathbf{I}(\boldsymbol{\theta})]_{p,q} = \frac{1}{\sigma^2}\sum_{n=1}^{N}\sum_{m=1}^{M}\left[\frac{\partial(\hat{x}^*_{m,n}(\boldsymbol{\theta}))}{\partial\theta_p}\frac{\partial(\hat{x}_{m,n}(\boldsymbol{\theta}))}{\partial\theta_q} + \frac{\partial(\hat{x}_{m,n}(\boldsymbol{\theta}))}{\partial\theta_p}\frac{\partial(\hat{x}^*_{m,n}(\boldsymbol{\theta}))}{\partial\theta_q}\right], \quad p,q = 1,2,\cdots,2\mathcal{K}, \tag{23}$$

where we let $\theta_p = d_p$ for $p = 1,\ldots,\mathcal{K}$ and $\theta_p = v_{(p-\mathcal{K})}$ for $p = \mathcal{K}+1,\ldots,2\mathcal{K}$. We proceed to derive the partial derivatives of $\hat{x}_{m,n}$ with respect to d_k and v_k in Eqns. (24) and (25), respectively.

$$\frac{\partial(\hat{x}_{m,n}(\boldsymbol{\theta}))}{\partial d_k} = a_{m,n}\rho_k\left(-j4\pi(m-1)\frac{\Delta f}{c}\right)e^{-j4\pi(m-1)\Delta f\frac{d_k}{c}}e^{j4\pi(n-1)\frac{v_k}{\lambda}T_s}, \tag{24}$$

$$\frac{\partial(\hat{x}_{m,n}(\boldsymbol{\theta}))}{\partial v_k} = a_{m,n}\rho_k\left(j4\pi(n-1)\frac{T_s}{\lambda}\right)e^{-j4\pi(m-1)\Delta f\frac{d_k}{c}}e^{j4\pi(n-1)\frac{v_k}{\lambda}T_s}. \tag{25}$$

The CRLB with respect to each estimator is represented by the respective diagonal element in the inverse Fisher information matrix, expressed as

$$\theta_k^{\mathrm{CRLB}} = [\mathbf{I}^{-1}(\boldsymbol{\theta})]_{kk}, \quad k = 1,\cdots,2\mathcal{K}. \tag{26}$$

4.2 Capacity-to-Error Ratio

In [16], the authors proposed a metric to evaluate the efficiency of an ISAC system, which maintains a equilibrium between capacity and the accuracy of sensing. This metric is determined by the capacity and ergodic Cramér-Rao bound. Inspired by [16], we employ the capacity-to-error ratio (CER) in this work as the performance metric, defined as

$$\mathrm{CER} = \frac{C}{\kappa + \mathrm{MSE}}, \tag{27}$$

where C represents the Shannon capacity, while κ is a constant assumed to be 0.1 in this paper, restricting the peak value of CER. Additionally, MSE represents the MSE of the estimation for either range or velocity. CER quantifies the capacity obtainable for each unit of sensing error, providing a comprehensive measure of communication and sensing performance for an ISAC system. In particular, decreased MSE contributes to an increase in CER.

5 Simulation Results and Discussions

The simulation focuses on a scenario involving a single target, although it should be noted that the proposed algorithm is applicable to multi-target scenarios as

well. The carrier frequency is 27.5 GHz, with a subcarrier spacing of 300 kHz. The symbol length is $T = 3.3$ μs, while the cyclic prefix is $T_{\text{cp}} = T/4 = 0.8$ μs. As a result, the overall duration of a complete OFDM symbol is $T_s = 4.2$ μs. Quadrature amplitude modulation (QAM) was employed.

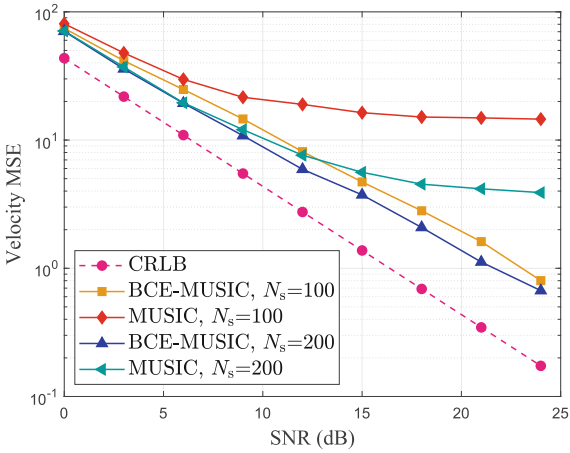

Fig. 3. MSE of estimated velocity values under different SNRs. The number of subcarriers is assumed to be $M = 8$. The number of OFDM symbols is assumed to be $N = 8$. The velocity of one target varies in $[-100, 100]$ m/s. The observation zone measures 6×6, represented as $N_d \times N_v = 6 \times 6$. N_{s} denotes the number of samples.

In Fig. 3, we studied how the SNR affected the MSE of estimated velocity values. The CRLB of OFDM-ISAC signal was given as the lower bound. Single target with mobility was uniformly distributed. It is observed that the MSEs of the MUSIC algorithm initially decrease and then reach a plateau due to the fixed number of samples in MUSIC spectra. Increasing the number of samples can help reduce the spacing of the MUSIC spectrum and improve the estimation accuracy at the expense of additional computational complexity. BCE-MUSIC with N_{s}=100 can achieve approximately 10 dB gain at SNR = 20 dB. It is worth noting that although our proposed method utilizes only a few samples of the MUSIC spectra, the MSE of BCE-MUSIC is close to that of CRLB derived from the entire received OFDM samples.

The relationship between CER and SNR with different M was discussed in Fig. 4. Similarly, CRLB indicated the theoretically lower bound. The range parameter is fixed to be $d_0 = 484$ m. As illustrated in Fig. 4, CER grows with the increasing SNR. In addition, increasing the number of subcarriers has exhibited significant improvements of CER due to the bandwidth and the improved ranging resolution. Moreover, it was noted that increasing the number of sampling points in the MUSIC spectrum leads to a reduction in the MSE of the BCE-MUSIC algorithm. Hence, CER could be improved.

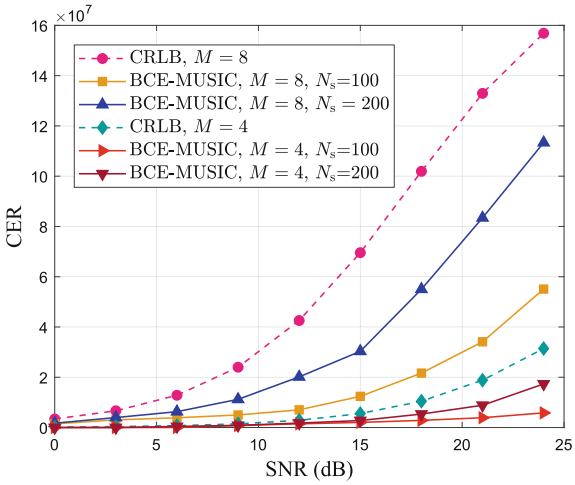

Fig. 4. CER versus SNR. The subcarrier space is $\Delta f = 300$ kHz and the size of two dimensional observation zone is $N_d \times N_v = 4 \times 4$. M denotes the number of subcarriers. N_s denotes the number of samples.

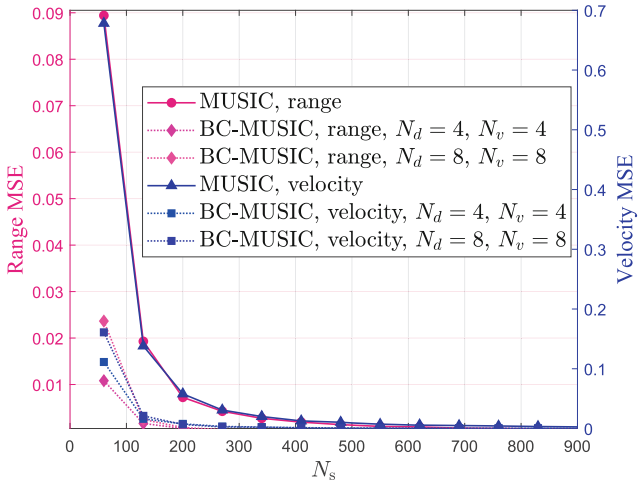

Fig. 5. MSE of range/velocity values versus the number of samples N_s. $f_c = 27.5$ GHz, $N = 4$, $M = 8$, $\Delta f = 300$ kHz. The number of samples in range/velocity dimensions varies from 60 to 900. The total count of Monte Carlo simulations is 200. The corresponding range varies in $[0, 62.5]$ m and the velocity varies in $[-81.8, 81.8]$ m/s.

As shown in Fig. 5, MSE decreased as the number of sampling points N_s increased. Note that the MSE was not normalized because the width of one index decreased when N_s increased. If normalized by one index, MSE does not decrease as N_s increases. More sampling points set within a fixed phase shift scope could

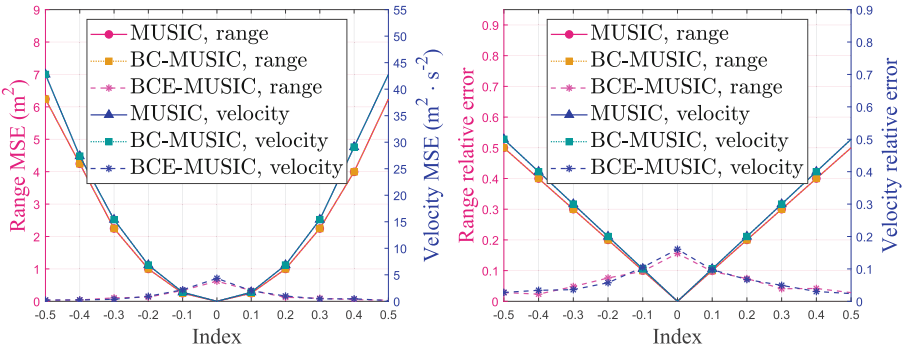

(a) MSE versus range and velocity of one index near the edge.

(b) Relative error versus range and velocity of one index near the edge.

Fig. 6. MSE/relative error versus range and velocity of one index near the edge. SNR is 24 dB and the number of samples is $N_s = 100$. Phase shift varies in $[0, 2\pi]$ and the corresponding range varies in $[2.4983, 7.4948]$ m. Velocity varies in $[-6.5409, 6.5409]$ m/s, and both of them fall near the edge. The observation zone measures 6×6, represented as $N_d \times N_v = 6 \times 6$.

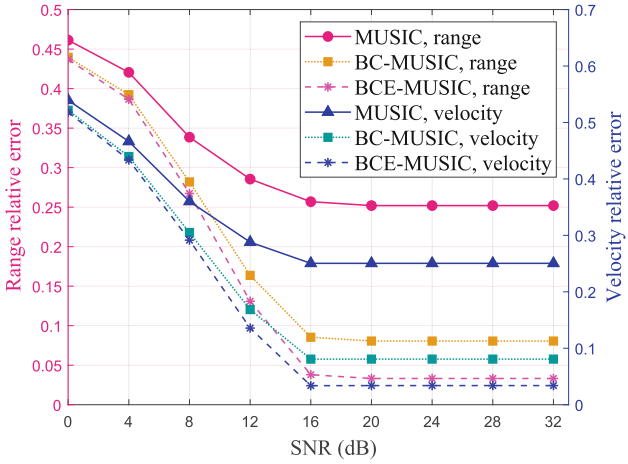

Fig. 7. Relative errors of range/velocity values versus SNR. Relative error refers to the difference between the estimated peak and the actual peak values, which varies in $0 \sim 0.5$. The number of samples $N_s = 50$ and the number of Monte Carlo simulations is 10000. The corresponding range varies in $[0, 490]$ m and velocity varies in $[-100, 100]$ m/s. The observation zone measures 6×6, represented as $N_d \times N_v = 6 \times 6$.

lead to the increasing complexity of the MUSIC algorithm. MSE reduction of both the MUSIC and BC-MUSIC algorithms becomes less evident as the number of sampling points grows. BC-MUSIC achieves a plateau with fewer sampling points compared to MUSIC. Consequently, the number of samples can be set

to maintain the trade-off between complexity and MSE. Additionally, as shown in Fig. 5, to reach the same range or velocity estimation accuracy, BC-MUSIC requires less sampling points N_s compared to the MUSIC algorithm. More sampling points lead to larger matrix operations that consume heavy computation resources, so BC-MUSIC possesses low complexity advantage compared with MUSIC algorithm.

The MUSIC, BC-MUSIC and BCE-MUSIC algorithms were evaluated. The range and velocity parameters were set based on one index on the spectrum near the edge. One index refers to the length between two sampling points of the spectrum. The Y-axis values of Fig. 6(a) and Fig. 6(b) are the MSE and the relative error, respectively. Relative error refers to the index difference between the estimating peak and the actual peak, which theoretically varies in $[0, 0, 5]$. Typical BC-MUSIC possesses the same performance with MUSIC due to the lack of careful coping with MUSIC spectrum edge. Owing to the fence effect, they could both achieve the lowest error at Index 0, where the actual peak falls exactly on a MUSIC sampling point. When the index moves near -0.5 or 0.5, larger error could be obtained as the actual peak moves away from a MUSIC sampling point. Nevertheless, the proposed BCE-MUSIC solved this problem and significantly reduced MSE/relative error. It is worth noting that BCE-MUSIC fails to reduce MSE when estimates are near a sampling point.

In Fig. 7, the relative errors of MUSIC algorithm are less than 0.5 when SNR is larger than 15 dB. Single target with range was uniformly distributed over $[0, 490]$ m, and velocity was uniformly distributed over $[-100, 100]$ m/s. The number of Monte Carlo simulations is 10000, which guarantees that sufficient targets fall near the edge. Relative errors are significantly reduced by using BC. However, BCE could further reduce the relative errors. Estimation accuracy could be further improved if the BCE algorithm is applied to the MUSIC spectrum.

6 Conclusion

This paper presents the BC-MUSIC algorithm, which is aimed at calibrating the MUSIC spectrum from the perspective of the super-resolution ISAC waveform. Under the constraints of available wireless resources, this algorithm improved the precision of range and velocity estimation at low complexity by calculating the barycenter of the spectrum. Furthermore, we considered how to accurately determine the barycenter on the asymmetric MUSIC spectrum when it is near the spectrum edge. Simulation results demonstrated that the presented algorithm achieves performance nearer to the Cramér-Rao Lower Bound (CRLB) and improves the capacity-to-error ratio (CER).

References

1. Sturm, C., Wiesbeck, W.: Waveform design and signal processing aspects for fusion of wireless communications and radar sensing. Proc. IEEE **99**(7), 1236–1259 (2011)
2. Zhang, R., Cheng, L., Wang, S., et al.: Integrated sensing and communication with massive MIMO: a unified tensor approach for channel and target parameter estimation. IEEE Trans. Wireless Commun. Early Access, 1 (2024)
3. Zheng, L., Wang, X.: Super-resolution delay-doppler estimation for OFDM passive radar. IEEE Trans. Signal Process. **65**(9), 2197–2210 (2017)
4. Liu, Y., Liao, G., Chen, Y., et al.: Super-resolution range and velocity estimations with OFDM integrated radar and communications waveform. IEEE Trans. Veh. Technol. **69**(10), 11659–11672 (2020)
5. Li, W., Liao, W., Fannjiang, A.: Super-resolution limit of the ESPRIT algorithm. IEEE Trans. Inf. Theory **66**(7), 4593–4608 (2020)
6. Xie, R., Hu, D., Luo, K., et al.: Performance analysis of joint range-velocity estimator with 2D-MUSIC in OFDM radar. IEEE Trans. Signal Process. **69**, 4787–4800 (2021)
7. Van Trees, H.L.: Detection, estimation, and modulation theory, part I: detection, estimation, and linear modulation theory. John Wiley & Sons, New York, NY, USA (2004)
8. Provencher, S.: Estimation of complex single-tone parameters in the DFT domain. IEEE Trans. Signal Process. **58**(7), 3879–3883 (2010)
9. Candan, C.: A method for fine resolution frequency estimation from three DFT samples. IEEE Signal Process. Lett. **18**(6), 351–354 (2011)
10. Macleod, M.D.: Fast nearly ML estimation of the parameters of real or complex single tones or resolved multiple tones. IEEE Trans. Signal Process. **46**(1), 141–148 (1998)
11. Quinn, B.G.: Estimating frequency by interpolation using Fourier coefficients. IEEE Trans. Signal Process. **42**(5), 1264–1268 (1994)
12. Quinn, B.G.: Estimation of frequency, amplitude, and phase from the DFT of a time series. IEEE Trans. Signal Process. **45**(3), 814–817 (1997)
13. Liu, X., Yang, Y., Gong, J., et al.: Amplitude barycenter calibration of delay-doppler spectrum for OTFS signal-an endeavor to integrated sensing and communication waveform design. IEEE Trans. Wireless Commun. **23**(4), 2622–2637 (2024)
14. Yang, Y., Pan, Y., Liu, X., et al.: Barycenter calibration with high order spectra of windowed delay-doppler signals for OTFS based ISAC systems. IEEE Trans. Signal Process. Early Access, 1–16 (2024)
15. Zhao, B., Yang, Y., Wang, Z., et al.: Barycenter calibration of spatial spectra for direction-of-arrival estimations based on Capon/MUSIC algorithms. IEEE Wireless Commun. Lett. **12**(12), 2068–2072 (2023)
16. Jiang J., Xu M., Zhao Z., et al.: Rethinking the performance of ISAC system: from efficiency and utility perspectives. In: Proceedings of the 1st ACM MobiCom Workshop on Integrated Sensing and Communications Systems, pp. 19–24. Association for Computing Machinery, Sydney, NSW, Australia (2022)